Interface Design Based on Strain Isolation Theory with Optimised Neutral Mechanical Plane Enables Highly Ductile and Flexible Organic Photovoltaics

Shumin Zeng, [a] Haojie Li, [a] Siqi Liu, [b] Tangyue Xue, [c] Kai Zhang, [d] Lin Hu, [e] Zheren Cai, [f] Yongting Cui, [a] Hanlin Wang, [a] Meng Zhang, [g] Xiaotian Hu,*[ah] Long Ye,*[d] Yanlin Song, [g] Yiwang Chen*[abh]

Materials and Methods

Materials

PM6, Y6, BTP-eC9, PY-IT, L8-BO and PDINN are purchased from Solarmer Materials Inc. PEDOT:PSS (Clevios PVP Al4083, Clevios PH1000) is obtained from Heraeus. CF (≥99%), Ethanol (99.9%), methanol (99.8%), and 1,8-Diiodooctane (DIO, 98%) are supplied by Sigma Aldrich. 1-chloronaphthalene (1-CN, 97%) are purchased from TCI.

Synthesis process of Poly(TA-DIB-Fe)

TA(Thioctic acid) powder (5 g) is added to a three-neck flask and then stirred under heating conditions in an oil bath at 90 ℃.TA is polymerized under heating conditions by ring-opening polymerization through disulfide bonds to give a yellow transparent low viscosity liquid, Poly(TA), after 30 min. During continuous stirring, 1 g of DIB (1,3-Diisopropenylbenzene) and 0.01 g of $FeCl_3$ are sequentially added to the Poly TA) solution, and the copolymerization is completed after 10 min. The liquid mixture is poured into a mold and cool to room temperature to obtain a transparent, flexible copolymer.

Measurements and instruments

Fabrication of organic solar cells

The organic solar cells are fabricated with a conventional architecture of glass/ITO/(Poly(TA-DIB-Fe))(5-15 nm)/PEDOT:PSS (40 nm)/active layer (100

nm)/PDINN (~15 nm)/Ag (100 nm). The glass substrate engraved with ITO is washed with detergent, deionized water and isopropyl alcohol under ultrasonic for 30 minutes each time, and then dried with a nitrogen gun. The Poly(TA-DIB-Fe)(0.1 mg/mL) is dissolved in ethanol and stirred at 60 ℃ for 2 hours. The solutions are spin-coated on ITO at 2000-4000 rpm for 40 s to obtain the films with a thickness of 5-15 nm. After the annealing at 100 ℃ for 10 min, the PEDOT:PSS is spin-coated at 4000 rpm (40 s) and generated at 150 °C in ambient atmosphere for 20 minutes. The active layer solution of PM6:Y6 (0.5% v/v CN) and PM6: BTP-eC9 (0.5% v/v DIO) are dissolves in CF at a total concentration of 16.5 mg/mL with the D/A ratio of 1:.2 by weight. The PM6:PY-IT are dissolved in CF (2% v/v CN) at a a total concentration of 14 mg/mL with the D/A ratio of 1:1.1 by weight. The PM6:BTP-eC9:L8-BO are dissolved in CF at the a concentration of 15 mg/mL with the D/A ratio of 1:0.4:0.8 by the weight. The solutions are stirred at 45 ℃ over 2 hours and then spin-coated on PEDOT:PSS layer at 3000 rpm for 60 s to obtain the films with a thickness of ~100 nm. Then the active layers are annealed at 90 ℃ for 10 min. The PDINN solution is dissolved in methanol by being stirred overnight and then spin coated on the active layer at 3000 rpm for 40 s. Finally, Ag (100 nm) is deposited as cathode through vacuum evaporation. The area of each device is 4 mm^2.

Fabrication of organic photovoltaics modules

Flexible organic photovoltaics modules are based on a PEN substrate with a blade coating process, solution preparation and annealing process consistent with small area photovoltaic devices. The ultra-flexible modules use a deposited PI film as the substrate, PH1000 as the transparent electrode, and the rest of the preparation processes are the same with the flexible modules. The organic solar module consists of seven sub-cells connected by laser etching, with a single cell size of 2.42 cm^2 (0.55 cm × 4.4 cm). In addition, the interconnections between the modules are shown in Fig. S21.

Encapsulation process of flexible organic photovoltaics

After confirming that the prepared device has no defects, the *J-V* curve is tested. In order to lead out the electrode wire a collector strip is attached at the common electrode. The butyl adhesive is attached around the front and back sides of the flexible device, and cut the POE of the corresponding size, lay the POE between the glass plate and the front and back of the device, cover the glass plate, and use the laminator for vacuum treatment.

Stability testing of flexible organic photovoltaics

Bending Stability

The bending stability of flexible organic solar cells is determined in nitrogen atmosphere with a bending radius of 2 mm.

Long-time Stability

The time stability of flexible organic solar cells is measured in a nitrogen atmosphere at 25 ℃ and 25% RH.

Characterizations

The current density-voltage (*J-V*) characteristics are characterized by a Keithley 2400 source meter. Standard silicon solar cells are calibrated by NREL and current is detected under a solar simulator (Enli Tech, 100 mW cm^{-2}, AM 1.5 G). The EQE spectra are recorded on a commercial EQE measurement system (Enlitech, QE-R3011) in nitrogen environment. The transient photocurrent (TPC) and photovoltage (TPV) are measured by the ABET TPV2000 in an air environment (25 °C, 20%-30% RH). The measurement system (Oriental spectra, NanoQ, NLD640) is equipped with a laser wavelength of 635 nm, a pulse width of < 12 ns and a spectral width of 2.7 nm. The ultraviolet-visible (UV-vis) spectra are measured by Agilent Tech. Inc. Cary 5000 spectrophotometer. The steady state photoluminescence (PL) spectrum is obtained

using a Shamrock sr-303i-B spectrograph from Andor Tech. PL spectra are excited using a Xe flash lamp. Fluorescence lifetime imaging microscopy (FLIM, FastFlim Q2, ISS lnc.) is scanned by PL Mapping in a 30×30 μm^2 area with an excitation wavelength of 532 nm. Grazing-incidence wide-angle X-ray scattering (GIWAXS) measurements are obtained at beamline BL02U2 of Shanghai Synchrotron Radiation Facility(SSRF). The incident angle is 0.16°, which maximized the scattering intensity from the samples, and the samples were radiated at the X-ray wavelength of 0.124 nm. The samples used for GIWAXS measurements are prepared on pure silicon substrates in a dimension of 1.5 cm×1.5 cm, and the conditions are the same as the device preparation. The surface morphology of films is measured by atomic force microscopy (AFM, MultiMode 8-HR (Bruker)) in tapping mode. The type of AFM cantilever is RTESPA-300, with a k constant of about 40 N/m. Since the test conditions are for thin films with a thickness of less than 100nm, images of Young's modulus, adhesion, and stiffness are all obtained simultaneously by AFM MultiMode 8-HR (Bruker) in PFQNM mode. The morphology of the PEDOT:PSS films is imaged by scanning electron microscope (SEM, JEOL, JSM-7500F, Japan) at an accelerating voltage of 5.0 kV. The tensile testing of the thin film is conducted using polydimethylsiloxane (PDMS) as the substrate. The thickness of the thin film is optimized to match the thickness of the highest PCE. The tensile deformation is set to 40%, which corresponds to the strain typically experienced by human skin during normal activities. The tensile testing is performed at a constant crosshead speed of 5 mm/min. The X-ray diffraction (XRD) measurements are performed using polyethylene naphthalate (PEN) as the substrate. The sample preparation conditions are identical to those used for device fabrication. Both control and target samples are subjected to 1000 bending cycles with a bending radius of 2 mm, consistent with the bending stability conditions.

Charge Carrier Mobility Measurements

The carrier mobility (hole and electron mobility) of photoactive active layer was obtained by fitting the dark current of hole/electron-only diodes to the space-charge-limited current (SCLC) model. Hole-only diode configuration: Glass/ITO/(Poly(TA-DIB-Fe)/PEDOT:PSS/active layer/MoO_3/Ag; Electron-only diode configuration: Glass/ITO/ZnO/active layer/PDINN/Ag

Supplementary note 1

Neutral mechanical plane of multilayer stacks

The neutral mechanical plane defines the position where the strains are zero. Figure S19 shows the multilayer stack with the 1st layer in ITO and the nth layer in Ag electrode. Their (plane-strain) moduli and thicknesses are denoted by E_1, … E_n and h_1, … h_n , respectively. The neutral plane is characterized by the distance b from the top surface, and b is given by

$$\boldsymbol{b} = \frac{\sum_{i=1}^{n} \boldsymbol{E_i h_i} \left[\left(\sum_j^i \boldsymbol{h_j} - \frac{\boldsymbol{h_i}}{\boldsymbol{2}} \right) \right]}{\sum_{i=1}^{n} \boldsymbol{E_i h_i}}$$

Functional layer

$$\boldsymbol{b} = \frac{\sum_{i=1}^{n} \boldsymbol{E_i}\, \boldsymbol{h_i} \left[\left(\sum_j^i \boldsymbol{h_j} \right) - \frac{\boldsymbol{h_i}}{\boldsymbol{2}} \right]}{\sum_{i=1}^{n} \boldsymbol{E_i h_i}}$$

$$= \frac{\boldsymbol{E_1 h_1} \left(\boldsymbol{h_1} - \frac{\boldsymbol{h_1}}{\boldsymbol{2}} \right) + \boldsymbol{E_2 h_2} \left[(\boldsymbol{h_1} + \boldsymbol{h_2}) - \frac{\boldsymbol{h_2}}{\boldsymbol{2}} \right] + \ldots + \boldsymbol{E_6 h_6} \left[(\boldsymbol{h_1} + \boldsymbol{h_2} + \ldots + \boldsymbol{h_6}) - \frac{\boldsymbol{h_6}}{\boldsymbol{2}} \right]}{\boldsymbol{E_1 h_1} + \boldsymbol{E_2 h_2} + \ldots + \boldsymbol{E_6 h_6}}$$

$$= \boldsymbol{128\ nm}$$

Encapsulated device

$$\boldsymbol{b} = \frac{\sum_{i=1}^{n} \boldsymbol{E_i}\, \boldsymbol{h_i} \left[\left(\sum_j^i \boldsymbol{h_j} \right) - \frac{\boldsymbol{h_i}}{\boldsymbol{2}} \right]}{\sum_{i=1}^{n} \boldsymbol{E_i h_i}}$$

$$= \frac{\boldsymbol{E_1 h_1} \left(\boldsymbol{h_1} - \frac{\boldsymbol{h_1}}{\boldsymbol{2}} \right) + \boldsymbol{E_2 h_2} \left[(\boldsymbol{h_1} + \boldsymbol{h_2}) - \frac{\boldsymbol{h_2}}{\boldsymbol{2}} \right] + \ldots + \boldsymbol{E_9 h_9} \left[(\boldsymbol{h_1} + \boldsymbol{h_2} + \ldots + \boldsymbol{h_9}) - \frac{\boldsymbol{h_9}}{\boldsymbol{2}} \right]}{\boldsymbol{E_1 h_1} + \boldsymbol{E_2 h_2} + \ldots + \boldsymbol{E_9 h_9}}$$

$$= \boldsymbol{1.8001 \times 10^6\ nm}$$

Supplementary note 2

To investigate the mechanical stability of different OSCs films, we use the finite-element method to simulate the deformation of OSCs films under bending. Firstly, the basic theories for finite-element simulation are discussed. The bending test: For the multilayer films, the relationship between film stress and curvature radius is shown in: equation (1)

$$\boldsymbol{\sigma_f = \frac{E_f h_f}{6(1-\vartheta_s)R}} \qquad (1)$$

σ_f is the value of stress, E_f is the Young's modulus of film, h_f is the thickness of film, υ_s is the poisson's ratio of film and R is curvature radius. The relationship of film stress and displacement: equation (2)

$$\boldsymbol{D_{ij} = \sum_{k=1}^{n} \int_{z_k}^{z_k+h_k} Q_{ij}^{(k)} z^2 \, dz} \qquad (2)$$

Where D_{ij} is bending rigidity of system, k is the number of films and Q_{ij} is strain under stress of k film. We can write the general control equation of film stress and deformational displacement: as equation (3)

$$\boldsymbol{D_{11}\frac{\delta^4 w}{\delta x^4} + 2(D_{12}+2D_{23})\frac{\delta^4 w}{\delta x^2 \delta y^2} + D_{22}\frac{\delta^4 w}{\delta y^4} - N_x\frac{\delta^2 w}{\delta x^2} - N_y\frac{\delta^2 w}{\delta y^2} - 2N_{xy}\frac{\delta^2 w}{\delta x \delta y} =}$$

$$\boldsymbol{\frac{\delta^2}{\delta x^2}(N_x)\frac{h}{2} + 2\frac{\delta^2}{\delta x \delta y}(N_{xy})\frac{h}{2} + \frac{\delta^2}{\delta y^2}(N_y)\frac{h}{2}} \qquad (3)$$

Supplementary Figures

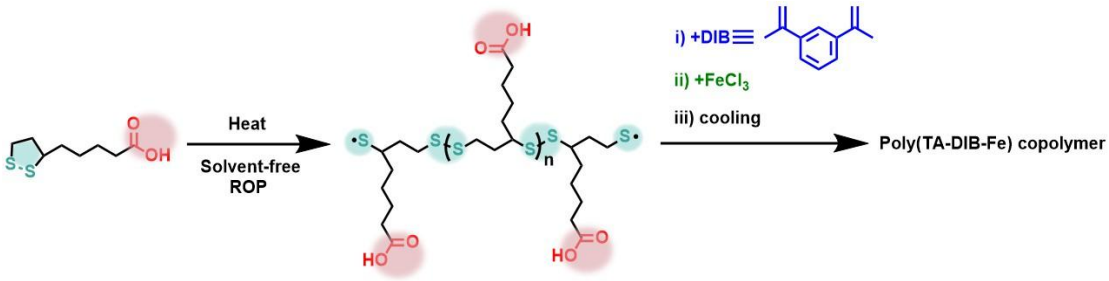

Supplementary Fig. 1 The synthesis process of Poly(TA-DIB-Fe).

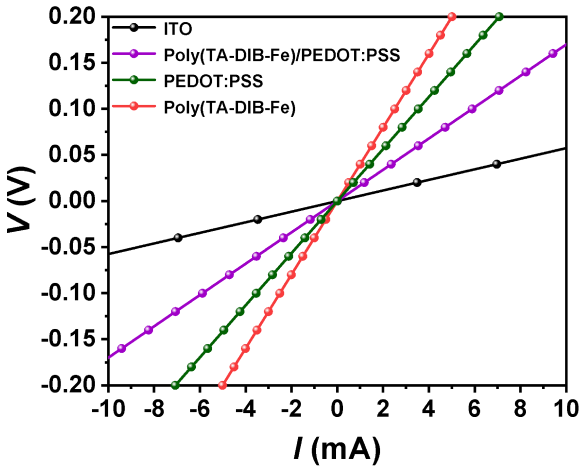

Supplementary Fig. 2 The conductivity of the films in the OSCs.

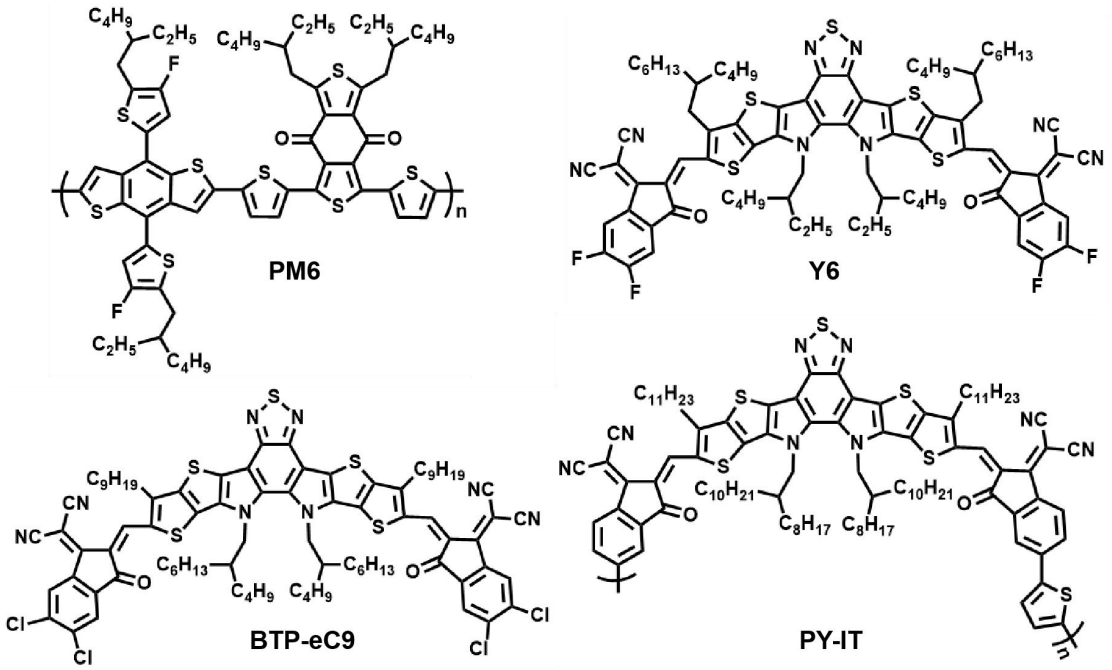

Supplementary Fig. 3 Chemical structure of PM6, Y6, BTP-eC9 and PY-IT.

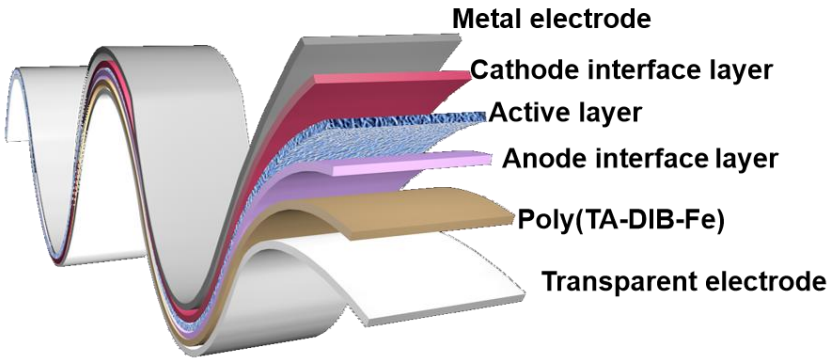

Supplementary Fig. 4 The diagrams of device structure of FOSCs.

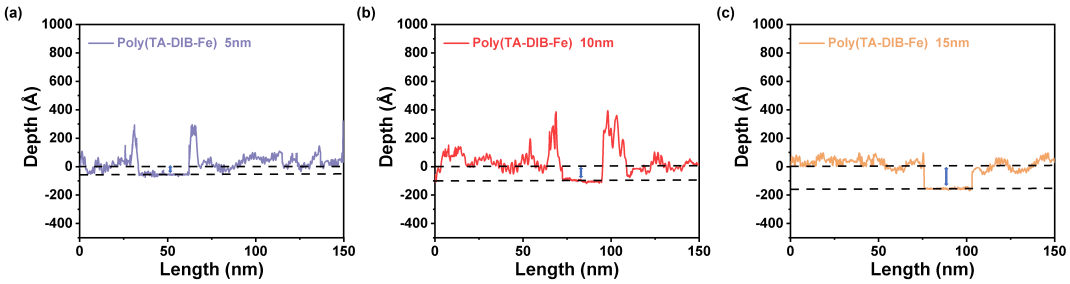

Supplementary Fig. 5 Thickness measured by a step profile system of the Poly(TA-DIB-Fe) film. The distance between the two dotted lines is the film thickness.

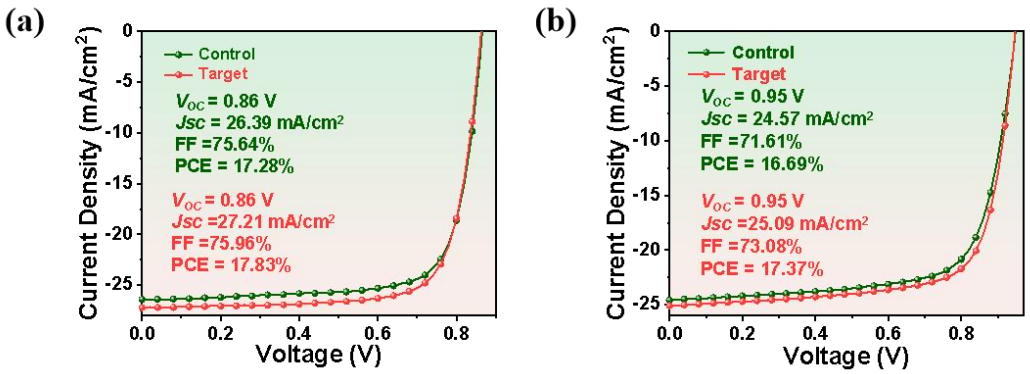

Supplementary Fig. 6 *J-V* curves of FOSCs devices based on PM6:Y6 (a) and PM6:PY-IT (b) with and without the Poly(TA-DIB-Fe).

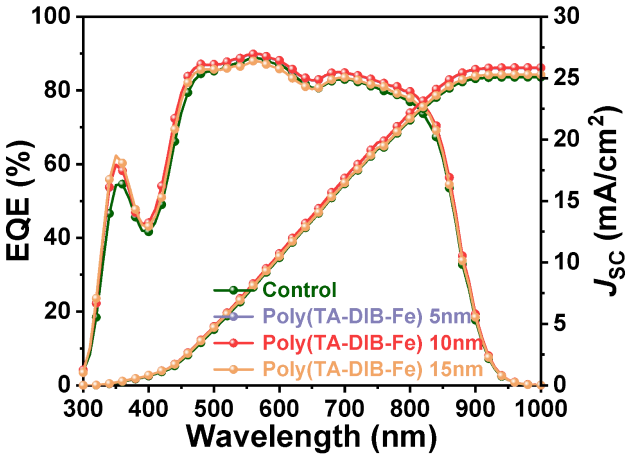

Supplementary Fig. 7 EQE spectra of FOSCs devices based on PM6:Y6 with different thickness of the Poly(TA-DIB-Fe).

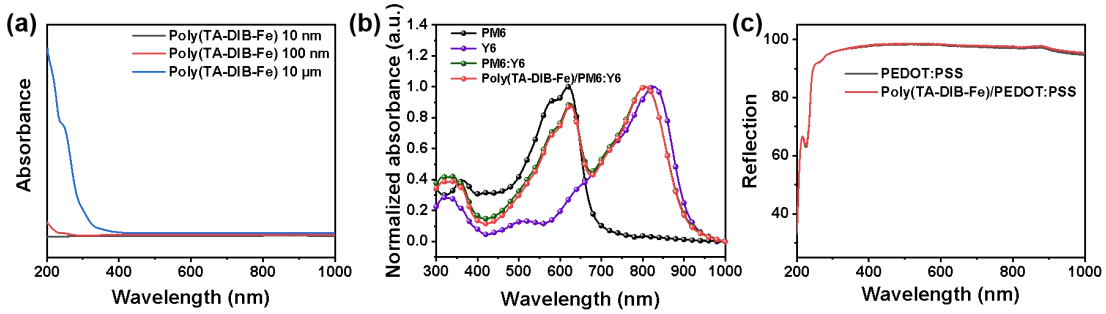

Supplementary Fig. 8 (a) UV-vis absorption spectra of different thickness of the Poly(TA-DIB-Fe) layer. (b) Normalized UV-vis absorption spectra of PM6, Y6, PM6:Y6 and Poly(TA-DIB-Fe)/PM6:Y6. (c) Reflection spectra of PEDOT:PSS films without and with the Poly(TA-DIB-Fe) layer.

As shown in Fig. S8a, the results demonstrate that as the film thickness increases, the color intensity of the film deepens, accompanied by an enhancement in absorption peaks within the 200-400 nm wavelength range. These findings underscore the thickness-dependent optical properties of Poly(TA-DIB-Fe), which are crucial for its application in optoelectronic devices. And the absorption curves in Supplementary Information Fig S8b are not significantly changed, which proves that the presence or absence of Poly(TA-DIB-Fe) layer has no effect on the optical properties of the PEDOT:PSS layer. Therefore, the added Poly(TA-DIB-Fe) layer does not act as an optical spacer. The Fig. S8c show that the reflectance curves of PEDOT:PSS with and without Poly(TA-DIB-Fe) layer are almost unchanged.

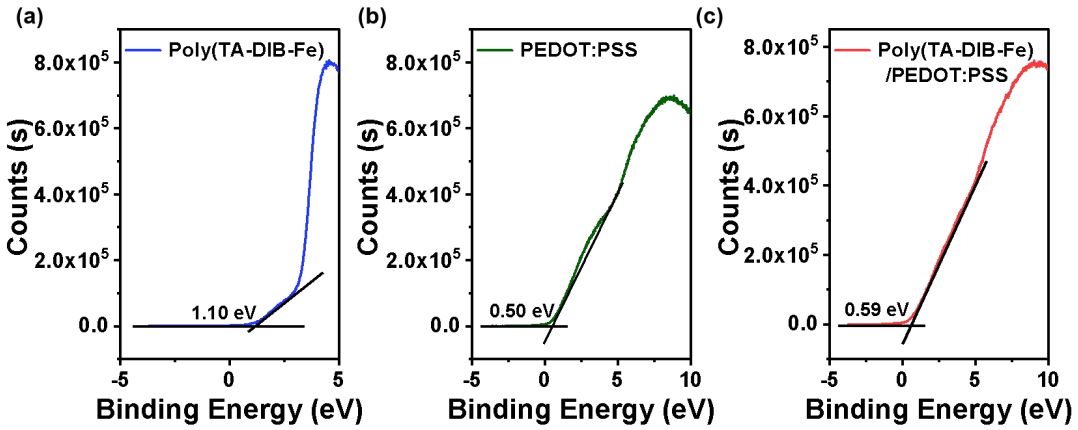

Supplementary Fig. 9 (a) UPS images of the Poly(TA-DIB-Fe) films. (b) UPS images of the PEDOT:PSS films and (c) PEDOT:PSS with the Poly(TA-DIB-Fe) layer .

The UPS test have added to get the energy levels of Poly(TA-DIB-Fe) films with the same thickness as used in the experimental conditions, as well as the changes in the energy levels of PEDOT:PSS films with and without the Poly(TA-DIB-Fe) layer. As shown in Fig. S9 and Table S2, it is evident that the energy levels of the Poly(TA-DIB-Fe) film are similar to the PEDOT:PSS film, and the addition of the Poly(TA-DIB-Fe) layer has minimal impact on the energy levels of the PEDOT:PSS film.

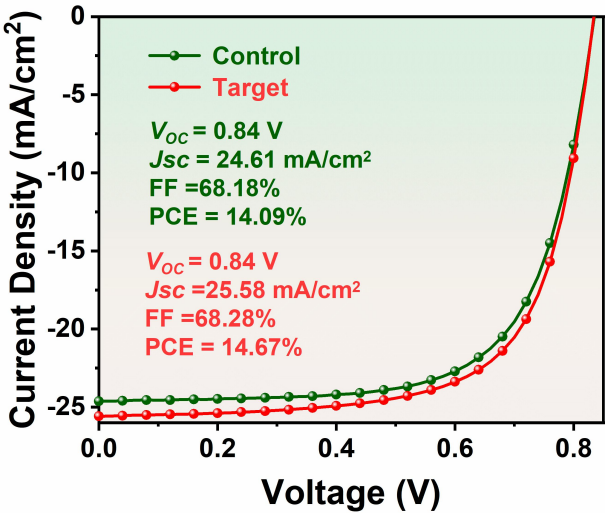

Supplementary Fig. 10 The *J-V* curves of the devices based on the structures of ITO/PM6:Y6/PDINN/Ag (control) and ITO/Poly(TA-DIB-Fe)/PM6:Y6/PDINN/Ag.

It can be seen that the PCE of the devices without the PEDOT:PSS layer is significantly lower than that of the devices with the PEDOT:PSS layer. However, the PCE trends are similar between the two groups. Additionally, the devices with the addition of the intermediate Poly(TA-DIB-Fe) layer show a certain degree of enhancement in J_{SC}.

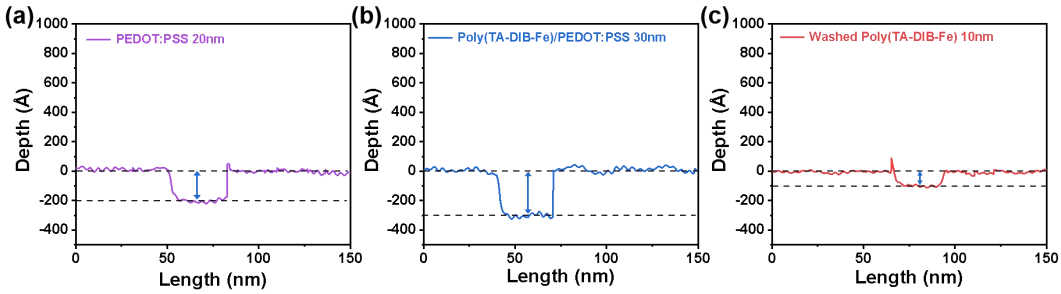

Supplementary Fig. 11 Thickness measured by a step profile system of the (a) PEDOT:PSS film. (b) Poly(TA-DIB-Fe)/PEDOT:PSS film. (c) Poly(TA-DIB-Fe) film after washing off PEDOT:PSS.

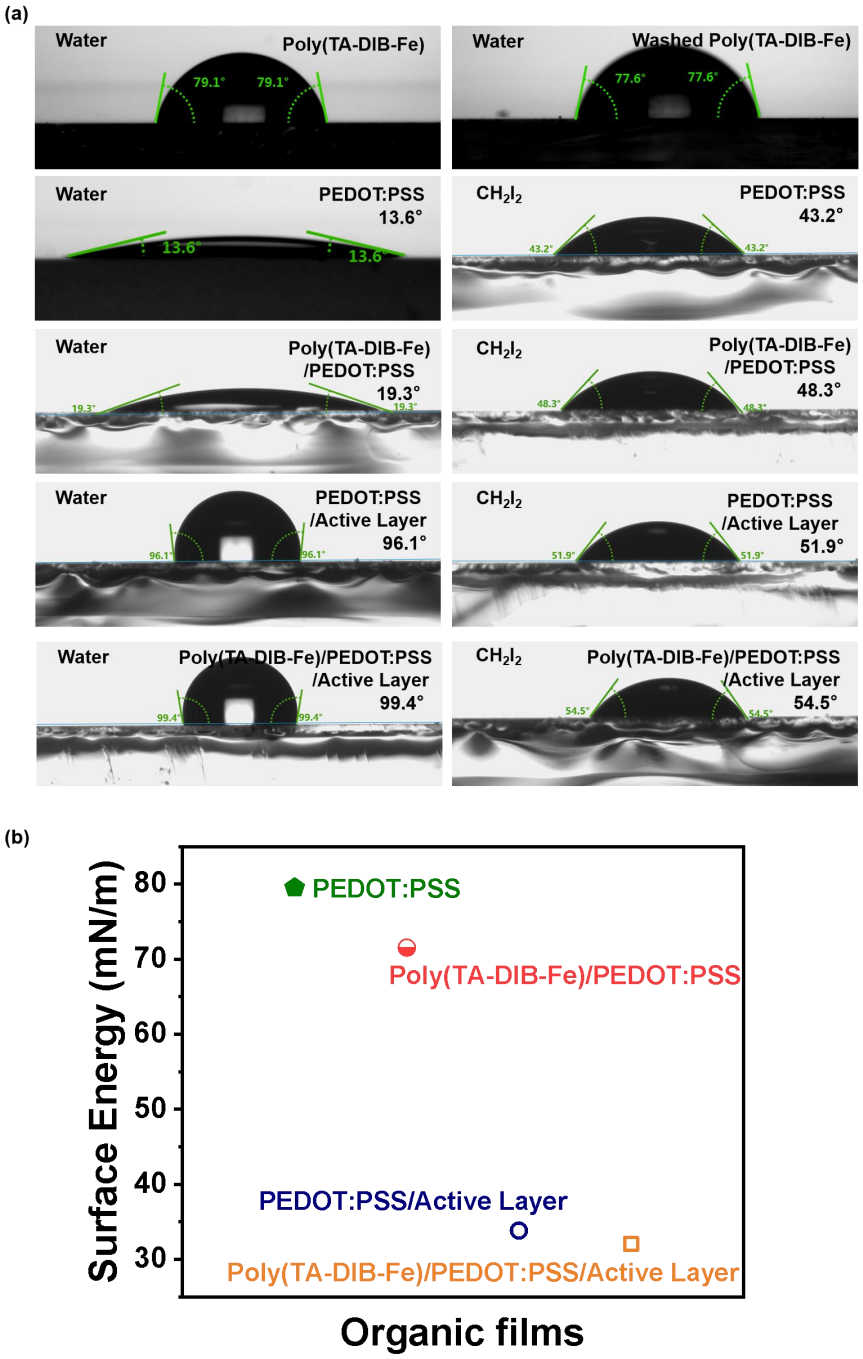

Supplementary Fig. 12 (a) Water contact angle images of films. (b) Surface energy of PEDOT:PSS and active layer films with or without the insert of the Poly(TA-DIB-Fe) layer.

The contact angle size of the Poly(TA-DIB-Fe) layer of the pure film is 79.1°, which is hydrophobic, whereas the PEDT:PSS film is hydrophilic with a contact angle size of only 13.6°, The contact angle size of the Poly(TA-DIB-Fe) layer remains 77.6°

after the PEDOT:PSS layer is washed away, which is close to that of the pure film, and it can be proved that there is no interaction between the two layers.

The change in surface energy is usually considered to be an optimisation of the crystallinity and morphology of the upper layer by the addition of the lower layer. The change in surface energy of the PEDOT:PSS layer before and after the insertion of the Poly(TA-DIB-Fe) intermediate layer could be calculated by dropping water and diiodomethane on the surface of PEDOT:PSS, respectively. As shown in Fig. S12, the insertion of the Poly(TA-DIB-Fe) intermediate layer decreases the surface energy of the PEDOT:PSS film, changing from 79.51° to 71.54°. The effect of the insertion of the Poly(TA-DIB-Fe) intermediate layer on the surface energy of the active layer is tested in the same way. It can be seen that there is almost no effect, but the surface energy of the PEDOT:PSS layer with the addition of the Poly(TA-DIB-Fe) intermediate layer matches more closely with the surface energy of the active layer film.

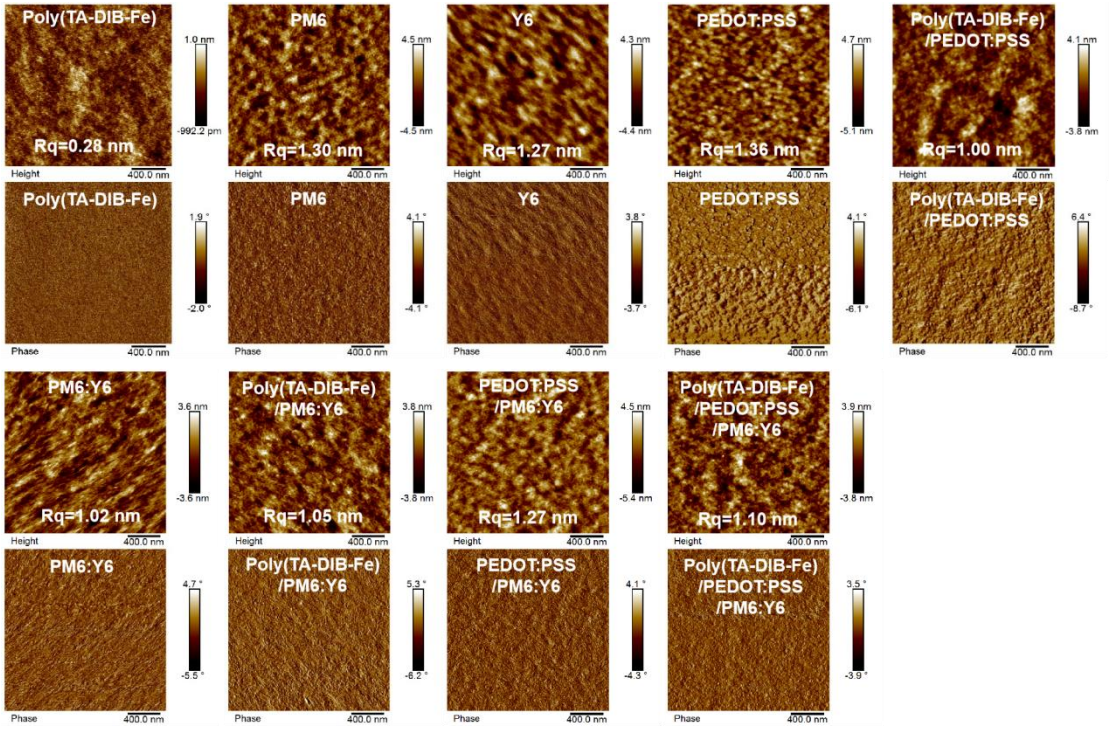

Supplementary Fig. 13 AFM height images and phase images of the films in OSCs.

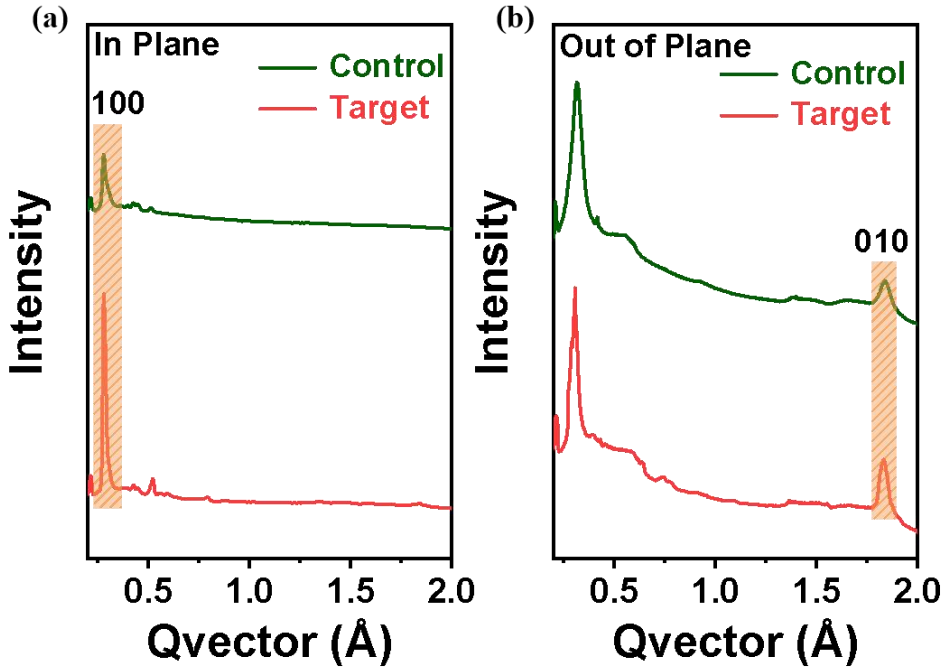

Supplementary Fig. 14 The corresponding (a) in-plane and (b) out-of-plane line profiles from the GIWAXS patterns of the PEDOT:PSS films without and with the Poly(TA-DIB-Fe) intermediate protective layer.

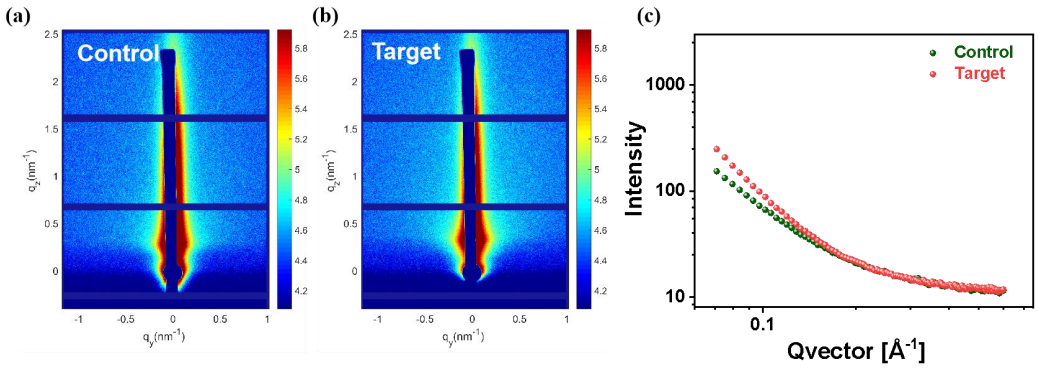

Supplementary Fig. 15 The 2D GISAXA patterns of the PEDOT:PSS films (a) without (b) and with the Poly(TA-DIB-Fe) layer. (c) The corresponding line profiles from the GISAXS patterns of the PEDOT:PSS films without and with the Poly(TA-DIB-Fe) layer.

In order to demonstrate that the crystallinity of PEDOT.PSS can be improved by the addition of a poly(TA-DIB-Fe) layer, GISAXS analyses of PEDOT:PSS films were performed. The insertion of Poly(TA-DIB-Fe) layer results in PEDOT:PSS films with higher intensities in the high scattering region and larger crystalline phase size.

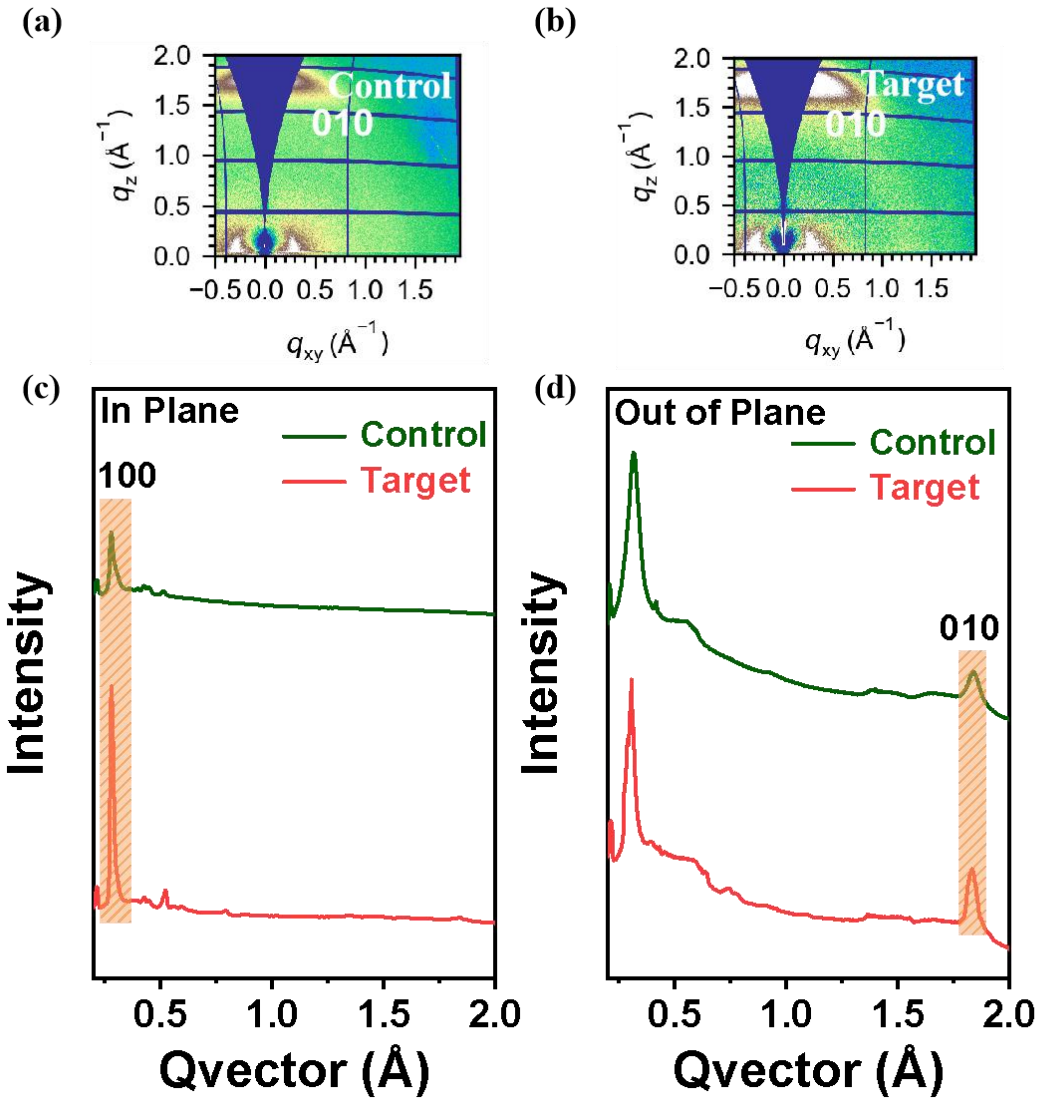

Supplementary Fig. 16 The 2D GISAXA patterns of the active layer films (a) without and (b) with the Poly(TA-DIB-Fe) layer. The corresponding (c) in-plane and (d) out-of plane line profiles from the GIWAXS patterns of the active layer films without and with the Poly(TA-DIB-Fe) layer.

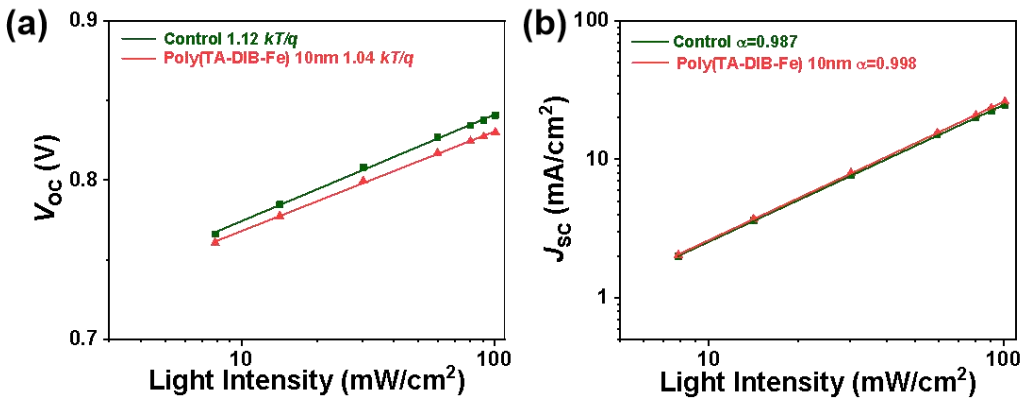

Supplementary Fig. 17 (a) The V_{OC} and (b) The J_{SC} versus light intensity of flexible devices based on PM6:Y6 without and with the Poly(TA-DIB-Fe) intermediate protective layer.

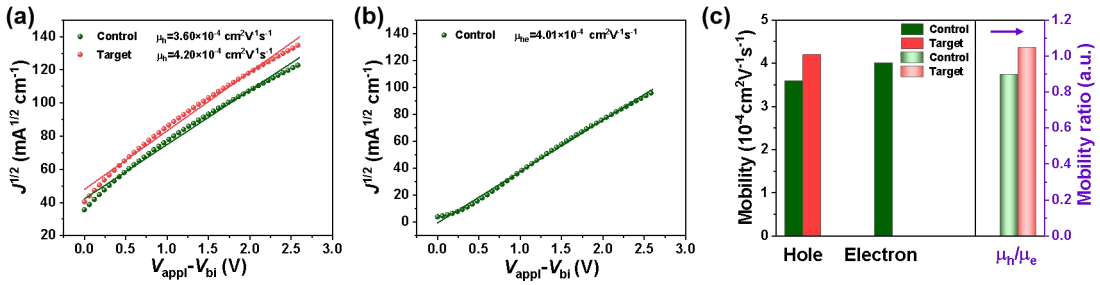

Supplementary Fig. 18 The hole and electron mobilities of the corresponding devices obtained from SCLC measurements.

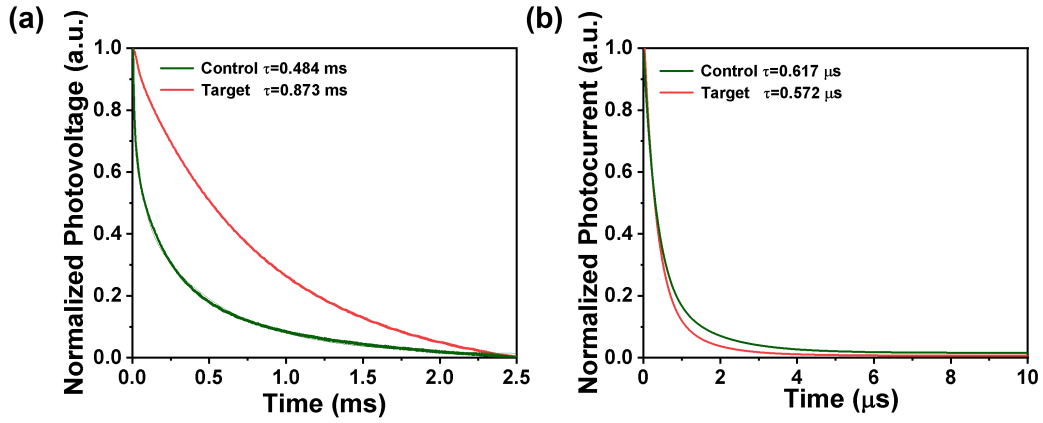

Supplementary Fig. 19 Normalized photovoltage decay and Normalized photocurrent decay of the devices without and with the Poly(TA-DIB-Fe) intermediate protective layer.

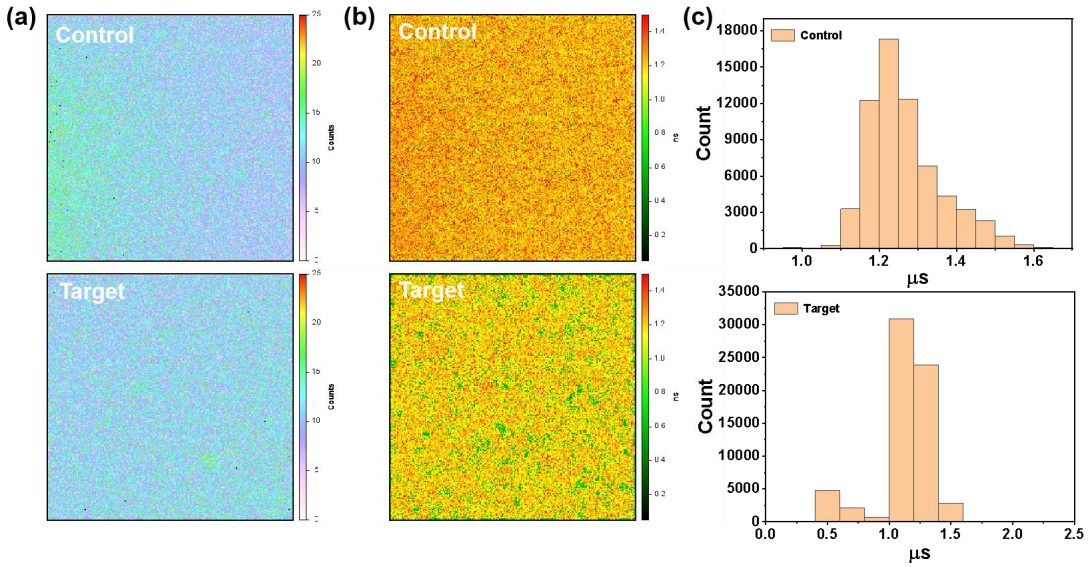

Supplementary Fig. 20 (a) The photoluminescence results of films based on PM6:Y6 without and with the Poly(TA-DIB-Fe) intermediate protective layer. (b) confocal PL lifetime imaging results of films based on PM6:Y6 without and with the Poly(TA-DIB-Fe) intermediate protective layer. (c) Histogram of confocal PL lifetime distribution.

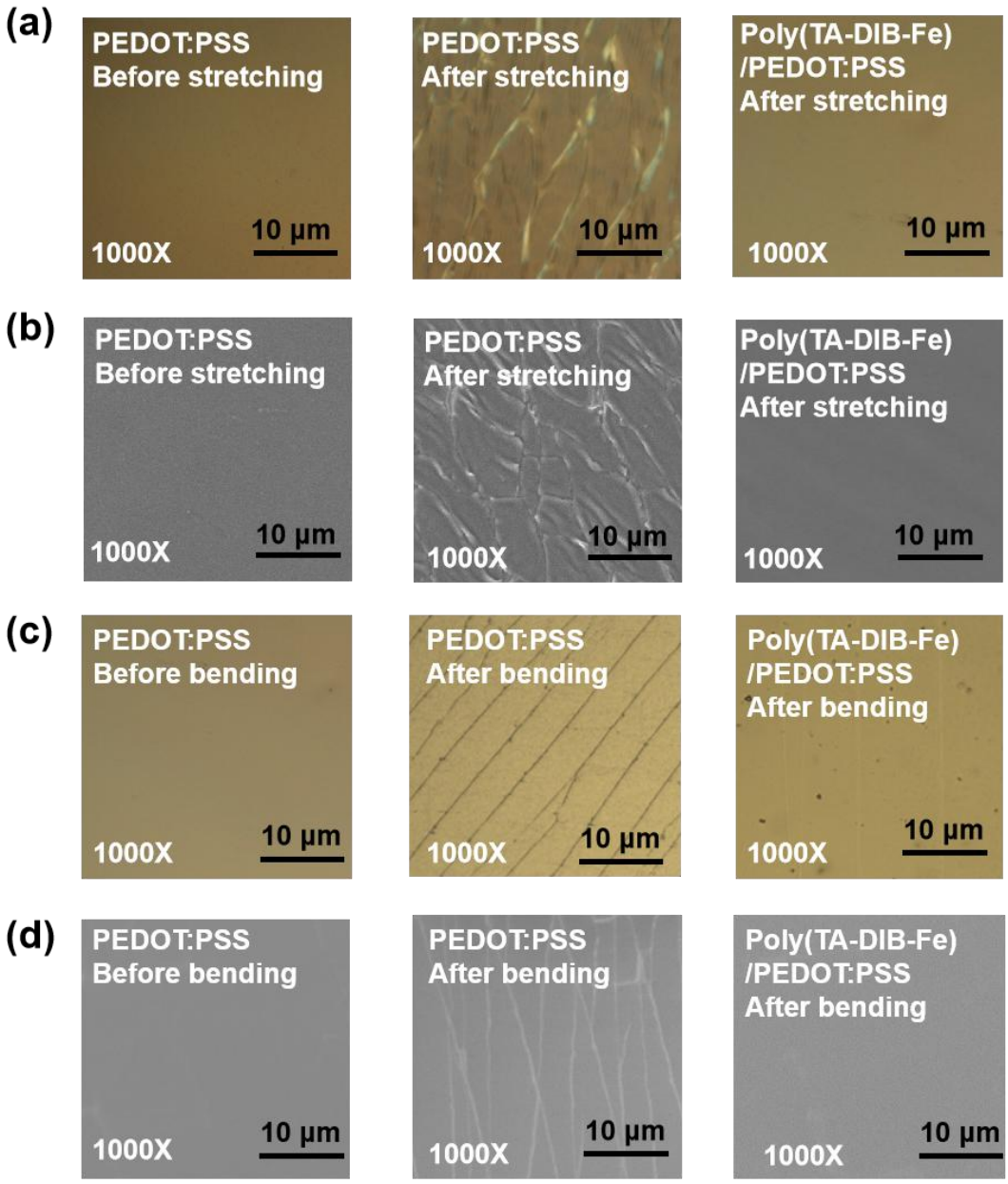

Supplementary Fig. 21 (a) OM and (b) SEM images of PEDOT:PSS films after stretching (40% strain) with and without the Poly(TA-DIB-Fe) intermediate protective layer. (c) OM and (d) SEM images of PEDOT:PSS films after bending with and without the Poly(TA-DIB-Fe) intermediate protective layer.

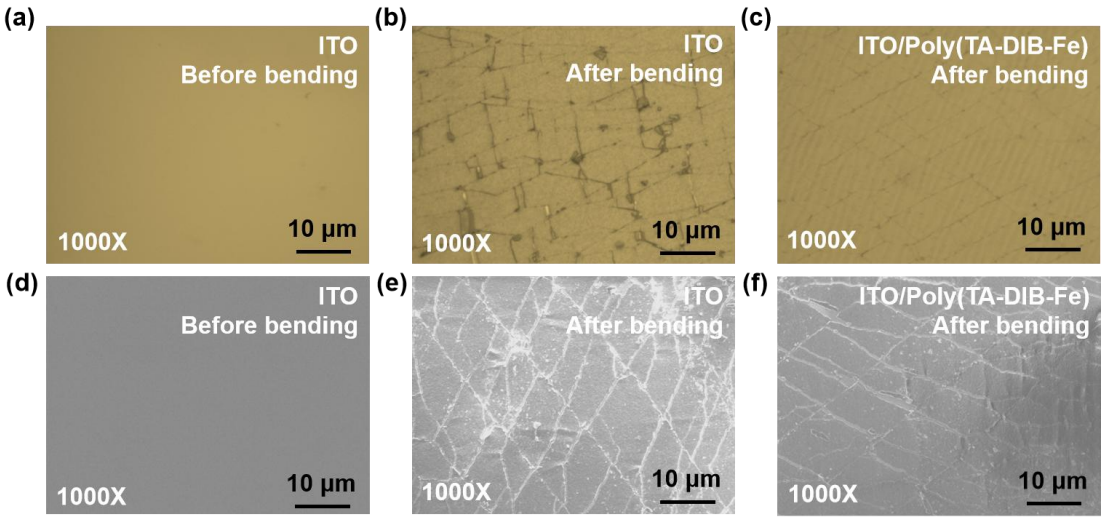

Supplementary Fig. 22 (a) OM and (d) SEM images of ITO before bending. (b) OM and (e) SEM images of ITO after bending without the Poly(TA-DIB-Fe) intermediate protective layer. (c) OM and (f) SEM images of ITO after bending with the Poly(TA-DIB-Fe) intermediate protective layer.

Analysed from the OM and SEM results, the ITO without Poly(TA-DIB-Fe) layer showed obvious cracking and partial detachment after bending, while the cracking phenomenon was obviously suppressed after inserting the Poly(TA-DIB-Fe) layer. It is proved that the addition of Poly(TA-DIB-Fe) layer can effectively release the stress applied during the bending process, reduce the actual stress applied to ITO, and improve its bending performance.

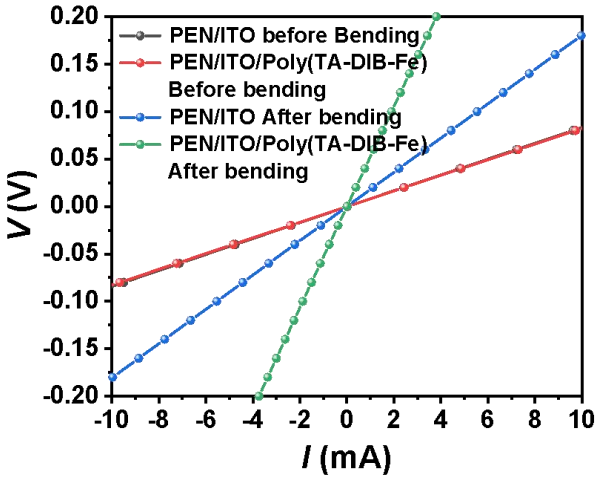

Supplementary Fig. 23 Conductivity *I-V* curves of PEN/ITO without and with Poly(TA-DIB-Fe) layer before and after bending.

From the analysis of the conductivity experimental results, ITO with or without Poly(TA-DIB-Fe) layer shows similar conductivity curves, and the conductivity of the pure ITO layer decreases significantly after bending, whereas the degree of decrease in conductivity is significantly improved after the Poly(TA-DIB-Fe) layer is inserted. It is demonstrated that the addition of Poly(TA-DIB-Fe) layer can reduce the generation of ITO cracks and maintain the integrity of the conductive path.

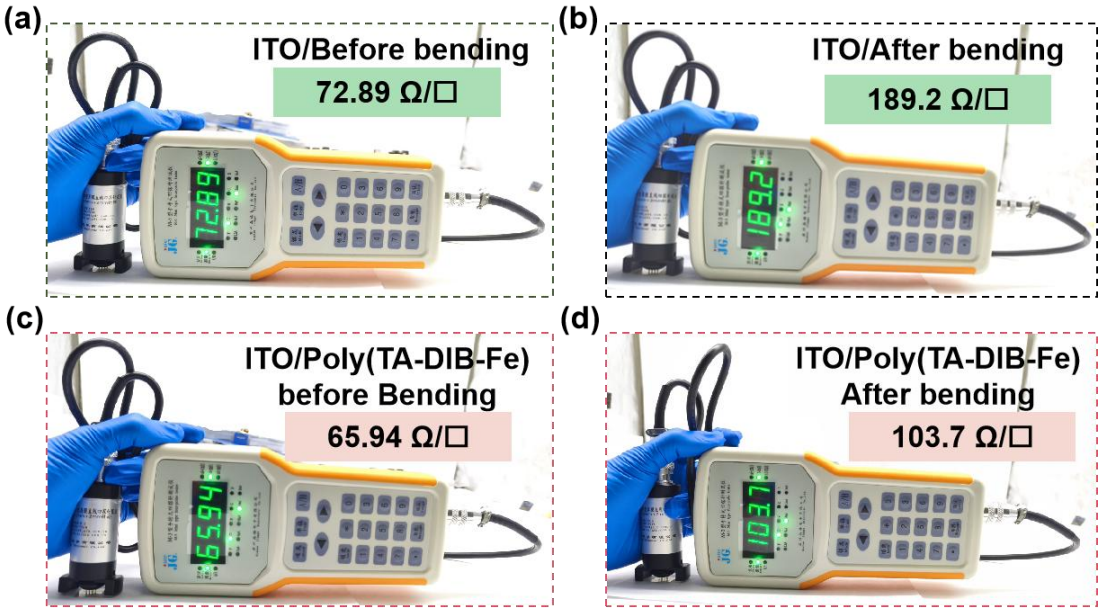

Supplementary Fig. 24 (a) PEN/ITO square resistance before bending. (b) PEN/ITO square resistance after bending. (c) PEN/ITO/Poly(TA-DIB-Fe) square resistance before bending. (d) PEN/ITO/Poly(TA-DIB-Fe) square resistance before bending.

From the analysis of the cube resistance experimental results, ITO with or without Poly(TA-DIB-Fe) layer exhibits similar cube resistance values, and the cube resistance of the pure ITO layer increases significantly after bending, while the degree of increase of the cube resistance decreases significantly after the insertion of Poly(TA-DIB-Fe) layer. Corresponding to the conductivity test results, the effect of Poly(TA-DIB-Fe) layer on ITO is further demonstrated.

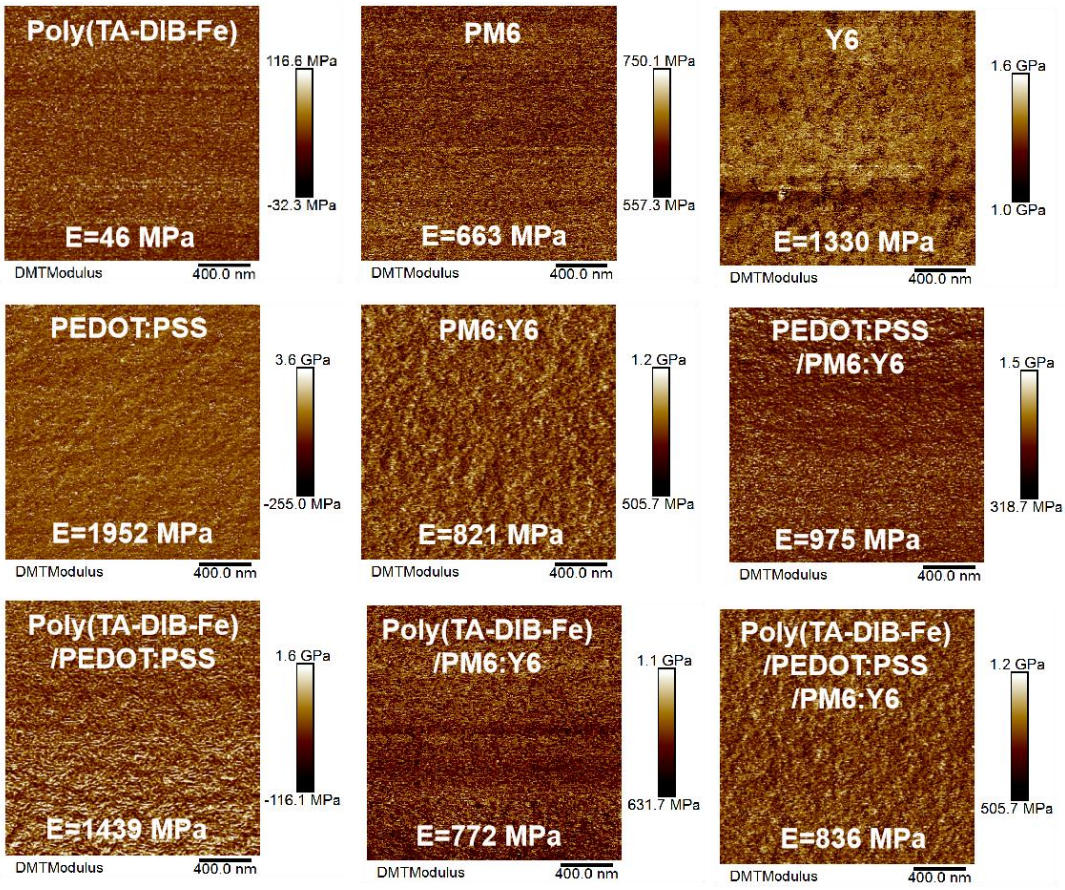

Supplementary Fig. 25 Young's modulus images of different films in OSCs.

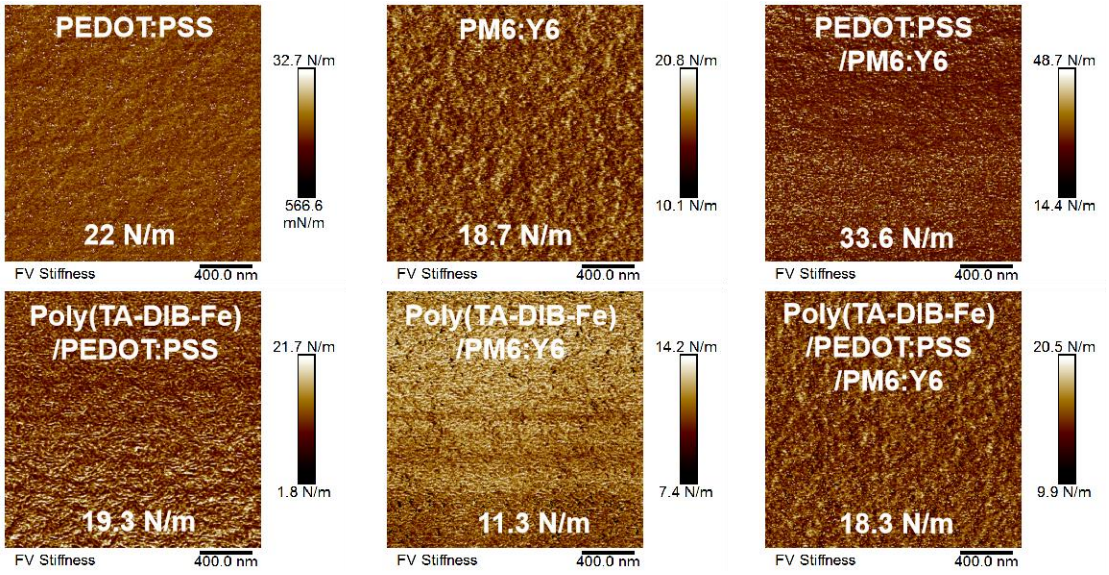

Supplementary Fig. 26 Stiffness images of different films in OSCs without and with the Poly(TA-DIB-Fe) intermediate protective layer.

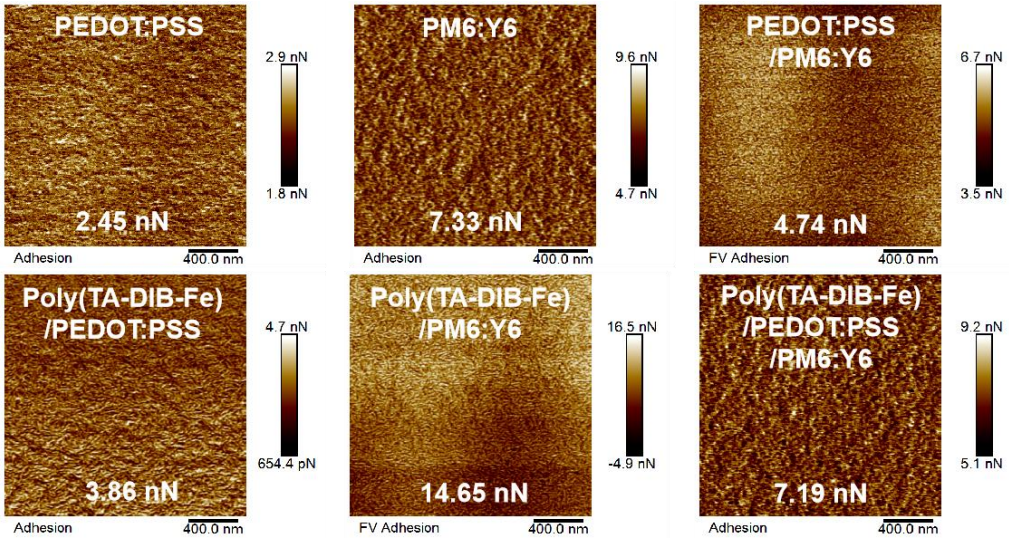

Supplementary Fig. 27 Adhesion images of different films in OSCs without and with the Poly(TA-DIB-Fe) intermediate protective layer.

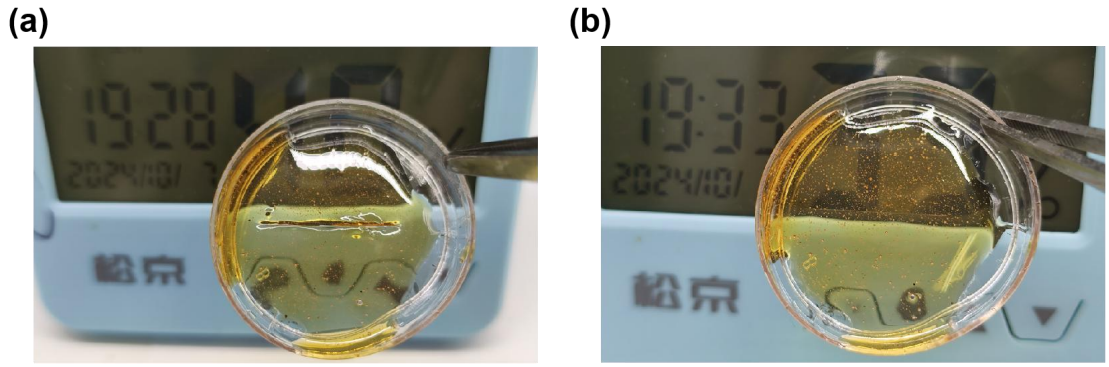

Supplementary Fig. 28 (a) The Poly(TA-DIB-Fe) film with scratches. (b) Self-healing scratch-healing Poly(TA-DIB-Fe) film under simulated solar illumination at room temperature.

The results show that Poly(TA-DIB-Fe) can complete self-healing in 5 minutes under simulated solar illumination at room temperature.

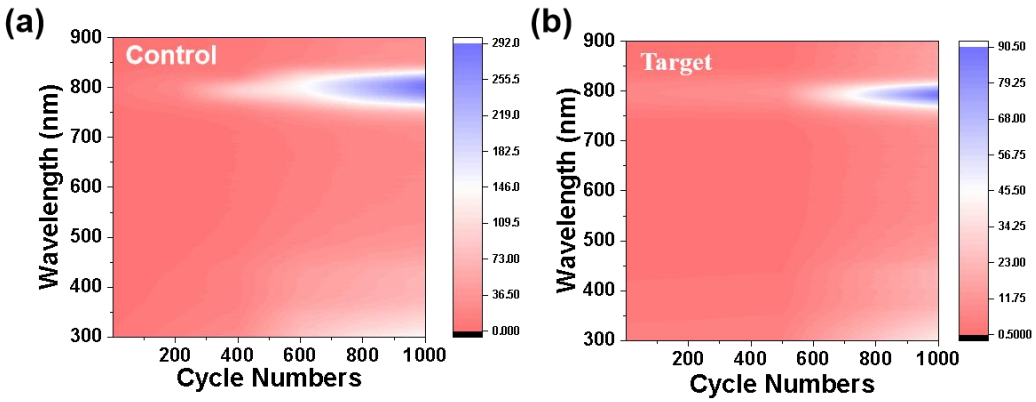

Supplementary Fig. 29 Mapping of steady-state PL of OSCs films without and with the Poly(TA-DIB-Fe) intermediate protective layer under different bending cycle numbers .

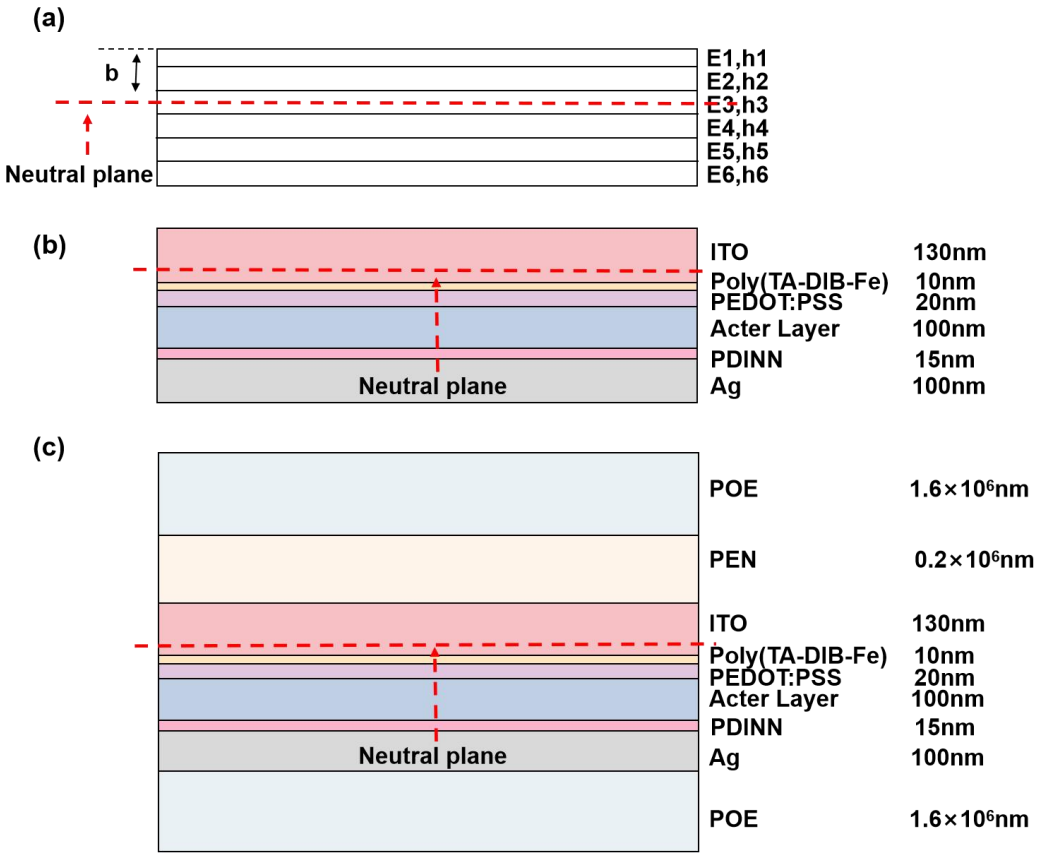

Supplementary Fig. 30 (a) Schematic diagram of a multilayer stack. (b) and (c) Neutral plane position of functional layers and neutral plane position of packaged devices with Poly(TA-DIB-Fe) intermediate protective layer.

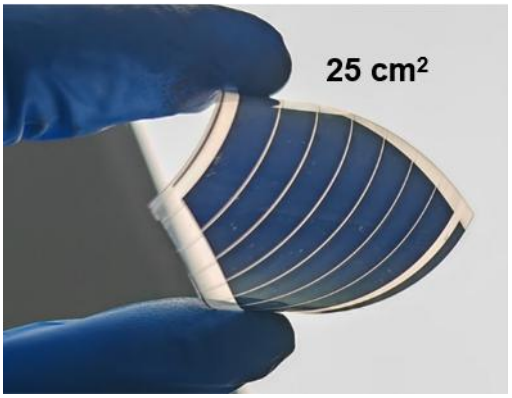

Supplementary Fig. 31 Photograph of the 25cm^2 flexible OPV modules based on PEN substrate.

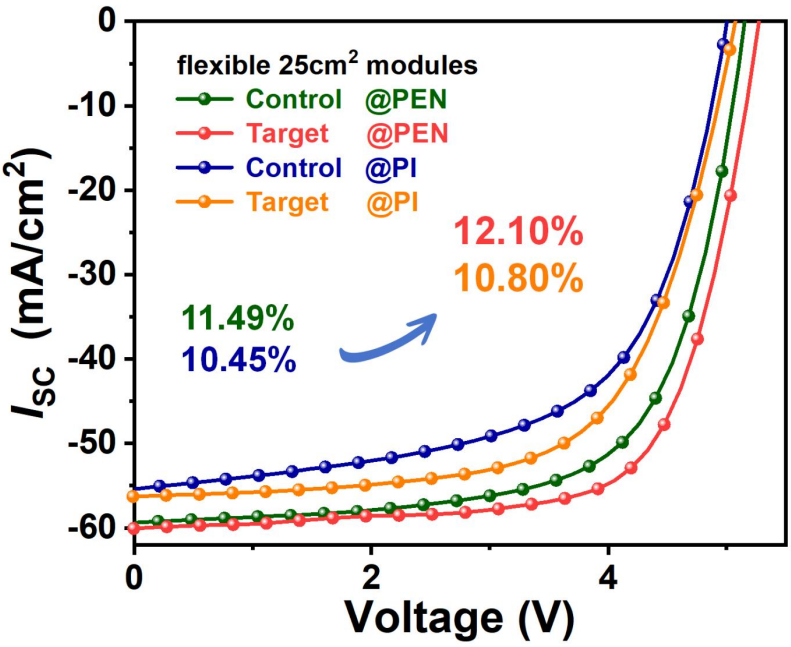

Supplementary Fig. 32 *I-V* curves of the 25cm^2 modules based on PEN and PI substrate without and with the addition of the Poly(TA-DIB-Fe) intermediate protective layer based on PM6:Y6 system.

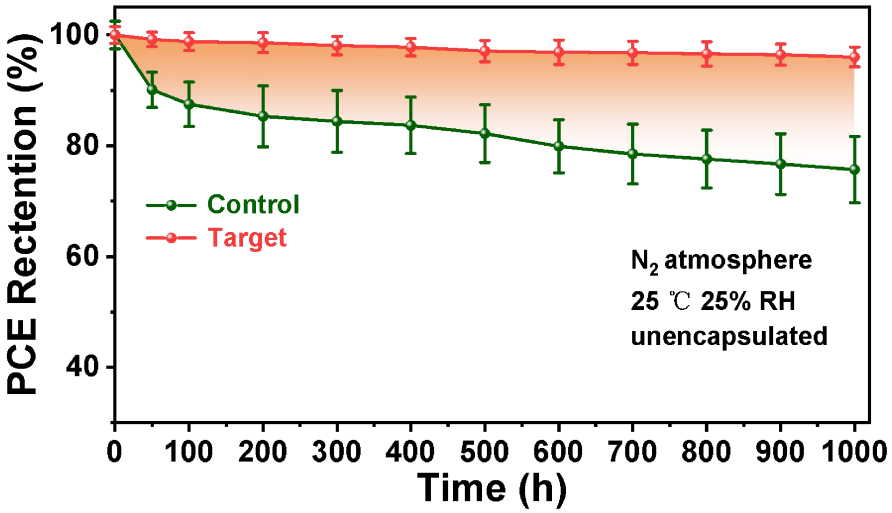

Supplementary Fig. 33 Stability characterization of the flexible OPV modules in N_2 atmosphere at 25 ℃ and 25% RH.

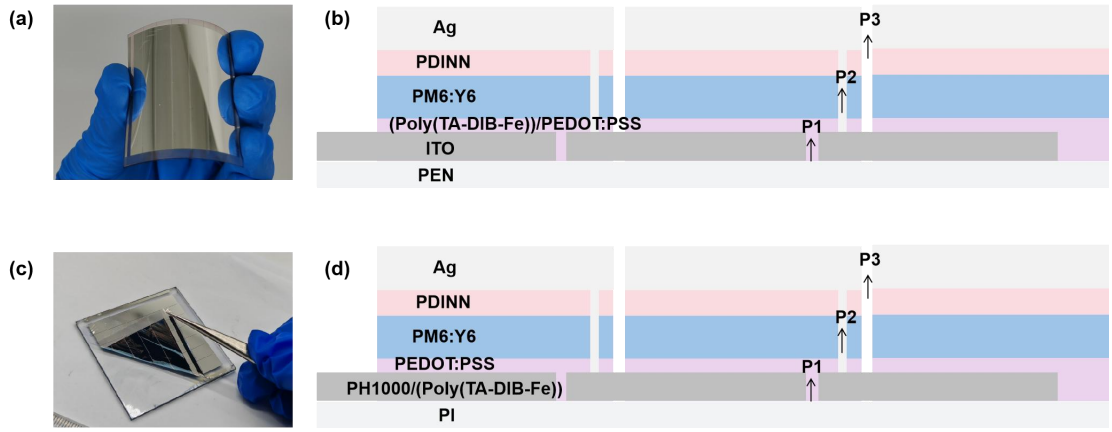

Supplementary Fig. 34 (a) Picture and (b) schematics diagram of OPV modules with the PEN as the substrate. (c) Picture and (d) schematics diagram of OPV modules with the PI as the substrate.

Supplementary Fig. 35 The geometric model of ultra-flexible OPV modules for bending simulation.

Supplementary Table 1. Photovoltaics parameters of different systems of FOSCs under simulated solar illumination (AM A.5G 100mW/cm^2)

Device	V_{OC} (V)	J_{SC} (mA/cm^2)	FF (%)	PCE (%)
Control[a)]	0.84 (0.838 ± 0.004)	25.51 (25.48 ± 0.25)	76.97 (76.85 ± 0.80)	16.48 (16.46 ± 0.18)
Poly(TA-DIB-Fe) 5 nm	0.84 (0.838 ± 0.005)	25.76 (25.70 ± 0.30)	77.70 (77.51 ± 0.76)	16.91 (16.88 ± 0.16)
Poly(TA-DIB-Fe) 10 nm	0.84 (0.838 ± 0.005)	26.27 (26.25 ± 0.28)	77.52 (77.86 ± 0.68)	17.19 (17.26 ± 0.13)
Poly(TA-DIB-Fe) 15 nm	0.83 (0.838 ± 0.005)	26.20 (26.12 ± 0.31)	76.84 (76.60 ± 0.76)	16.93 (16.88 ± 0.15)
Control[b)]	0.86 (0.860 ± 0.004)	26.39 (26.37 ± 0.35)	75.64 (75.55 ± 0.70)	17.28 (17.20± 0.17)
Target	0.86 (0.860 ± 0.004)	27.21 (27.14 ± 0.30)	75.96 (75.74 ± 0.66)	17.83 (17.77 ± 0.15)
Control[c)]	0.95 (0.948 ± 0.005)	24.57 (24.50 ± 0.37)	71.61 (71.58 ± 0.78)	16.69 (16.67 ± 0.16)
Target	0.95 (0.949 ± 0.004)	25.09 (25.07 ± 0.33)	73.08 (72.97 ± 0.60)	17.37 (17.31 ± 0.16)

The average parameters are calculated from 10 independent devices.

a) The devices based on PM6:Y6 system.

b) The devices based on PM6:BTP-eC9 system.

c) The devices based on PM6:PY-IT system.

Supplementary Table 2. UPS test results for the work function and HOMO energy levels of the Poly(TA-DIB-Fe) and the PEDOT:PSS films without and with the Poly(TA-DIB-Fe) layer.

	Work Function (eV)	HOMO (eV)
Poly(TA-DIB-Fe)	4.00	5.10
PEDOT:PSS	4.55	5.05
Poly(TA-DIB-Fe)/PEDOT:PSS	4.49	5.07

Supplementary Table 3 Photovoltaics parameters of different structures of FOSCs devices under simulated solar illumination (AM A.5G 100mW/cm^2).

	V_{OC}	J_{SC}	*FF*	PCE
Control[a)]	0.88 (0.880 ± 0.003)	24.61 (24.72 ± 0.34)	68.18 (68.54 ± 0.71)	14.09 (14.21 ± 0.24)
Target[b)]	0.88 (0.880 ± 0.004)	25.58 (25.79 ± 0.28)	68.28 (68.66 ± 0.68)	14.67 (14.80 ± 0.23)

The average parameters are calculated from 10 independent devices.

a) The FOSCs devices based on the structure of ITO/Active Layer/PDINN/Ag.

b) The FOSCs devices based on the structure of ITO/Poly(TA-DIB-Fe)/Active Layer/PDINN/Ag.

Supplementary Table 4. The parameters of the GISAXS of the PEDOT:PSS films without and with the Poly(TA-DIB-Fe) layer.

	ξ (nm)	η (nm)	D	$2R_g$ (nm)
Control	41.6	7.1	2.7	31.74
Target	32.3	9.4	2.8	43.36

where ξ is the disordered phase and 2Rg is the highly crystalline phase, indicating that the insertion of Poly(TA-DIB-Fe) layer results in PEDOT:PSS films with higher intensities in the high scattering region and larger crystalline phase size.

Supplementary Table 5. The location of (010) peaks, d-spacing, FWHM and CL values in the out-of-plane direction.

Direction		π-π stack (010)			
		Scattering vector (q) [Å^{-1}]	d-spacing [Å]	FWHM[a)]	CL (nm)
Out-of-plane	Control[b)]	1.795	3.50	0.318	17.8
	Target	1.790	3.51	0.304	18.6
	Control[c)]	1.760	3.57	0.272	20.8
	Target	1.755	3.58	0.262	21.6

a) FWHM is full width at half maximum of the scattering peak.

b) The PEDOT:PSS films without and with the Poly(TA-DIB-Fe) layer.

c) The PEDOT:PSS/Active Layer films without and with the Poly(TA-DIB-Fe) layer.

Supplementary Table 6. Young's modulus parameters of the films of OSCs.

	Young's Modulus (MPa)
Poly(TA-DIB-Fe)	46
PM6	663
Y6	1330
PEDOT:PSS	1952
PM6:Y6	821
Poly(TA-DIB-Fe)/PM6:Y6	772
Poly(TA-DIB-Fe)/PEDOT:PSS	1439
PEDOT:PSS/PM6:Y6	975
Poly(TA-DIB-Fe)/PEDOT:PSS/PM6:Y6	828

Supplementary Table 7. Young's modulus parameters and thickness of the layers of OSCs.

Layers		h/nm	E/GPa
1	ITO	130	170
2	Poly(TA-DIB-Fe)	10	0.05
3	PEDOT:PSS	20	2
4	Active Layer	100	0.8
5	PDINN	15	2.6
6	Ag	100	70

Supplementary Table 8. Young's modulus parameters and thickness of the layers of OSCs.

Layers		h/nm	E/GPa
1	POE	1.6×10^6	1
2	Poly(TA-DIB-Fe)	0.2×10^6	6
3	ITO	130	170
4	Poly(TA-DIB-Fe)	10	0.05
5	PEDOT:PSS	20	2
6	Active Layer	100	0.8
7	PDINN	15	2.6
8	Ag	100	70
9	POE	1.9×10^6	1

Supplementary Table 9. Mechanical properties of each functional film for finite-element simulation.

Materials	thickness (μm)	Young's modulus (MPa)	Density (ρ, g/cm^3)	Poisson's ratio
PM6:Y6	0.1	80	1.77	0.35
PEDOT:PSS	0.02	200	1.39	0.32
PH1000	0.1	195	1.37	0.32
Poly(TA-DIB-Fe)	0.01	50	17.77	0.5

Supplementary Movie 1. The video shows that the mass of the prepared 25cm^2 ultra-flexible OPV module is only 24.56 mg.

Supplementary Movie 2. The video shows that the prepared 25cm^2 ultra-flexible OPV module can light up a small bulb after crumpling test.

Supplementary Movie 3. The video shows that the prepared 25cm^2 ultra-flexible OPV module is used to power a simple electrocardiograph (ECG).